Theory of kinetic arrest, elasticity, and yielding in dense binary mixtures of rods and spheres

Ryan Jadrich[1,3] and Kenneth S. Schweizer[1,2,3,*]

[1]*Department of Chemistry, University of Illinois, Urbana, Illinois 61801, USA*
[2]*Department of Materials Science, University of Illinois, Urbana, Illinois 61801, USA*
[3]*Frederick Seitz Materials Research Laboratory, University of Illinois, Urbana, Illinois 61801, USA*

We extend the quiescent and stressed versions of naïve mode coupling theory to treat the dynamical arrest, shear modulus, and absolute yielding of particle mixtures where one or more species is a nonrotating nonspherical object. The theory is applied in detail to dense isotropic "chemically matched" mixtures of variable aspect ratio rods and spheres that interact via repulsive and short range attractive site-site pair potentials. A remarkably rich ideal kinetic arrest behavior is predicted with up to eight "dynamical phases" emerging: an ergodic fluid, partially localized states where the spheres remain fluid but the rods can be a gel, repulsive glass or attractive glass, doubly localized glasses and gels, a porous rod gel plus sphere glass, and a narrow window where a type of rod glass and gel localization coexist. Dynamical complexity increases with rod length and the introduction of attractive forces between all species which both enhance gel network formation. Multiple dynamic reentrant features and triple points are predicted, and each dynamic phase has unique particle localization characteristics and mechanical properties. Orders of magnitude variation of the linear shear modulus and absolute yield stress are found as rod length, mixture composition and the detailed nature of interparticle attractions are varied. The interplay of total (high) mixture packing fraction and composition at fixed temperature is also briefly studied. The present work provides a foundation to study more complex rod-sphere mixtures of both biological and synthetic interest that include physical features such as interaction site size asymmetry, rod-sphere specific attractions, and/or Coulomb repulsion.

I. INTRODUCTION

Dense colloidal and nanoparticle suspensions of diverse and tunable properties are ubiquitous in synthetic and biological systems. Particles employed in materials applications span a wide range of sizes (nanometers to microns), shapes (e.g., spheres, rods, sheets, molecular clusters), and chemistry (e.g., silica, metals, glassy polymers, inorganic semiconductors) [1]. A similar diversity exists in the biological realm, e.g., globular proteins, rodlike and semiflexible biopolymers such as F-actin, and microtubules [2]. A vast array of mixtures is also important, from rod-sphere systems [3] such as biopolymer-protein networks, to "biphasic" mixtures of hydrophobic and hydrophilic silica colloids [4]. A recent powerful materials application is the direct write printing of durable conductive electrodes in fragile electronic devices such as solar microcells based on extruding a metallic nanosphere gel or a nanosphere-nanowire mixture [5]. Such materials applications often require simultaneously tailoring statistical structure, electrical transport, and viscoelastic properties including shear elasticity and yielding response under high solids loading conditions.

The mechanical properties of kinetically arrested synthetic particle systems depend on many controllable variables such as interparticle forces, relative concentrations, temperature, particle shapes, and total particle packing fraction. The shear elasticity of these systems in amorphous glasses and gels is intimately related to the physical nature of the localized state and intermolecular structure. For one-component spherical particle systems, repulsive glasses, gels, and attractive glasses can be formed, each with its own unique viscoelastic properties

[6–10], where particle localization is the result of repulsive-force caging, physical bonding due to strong short range attractions, and a mixture of caging and bond formation, respectively. Besides attractions, particle shape anisotropy affords another tunable route for realizing novel kinetically arrested states with distinctive mechanical properties. For example, recent experimental [11] and theoretical [12–14] studies of one-component suspensions of low aspect ratio dicolloids has discovered they can form plastic glasses (only translation arrested), double glasses (arrested translation and rotation), or double gels. The kinetic arrest phenomenon and mechanical properties of this system are well described [11,14,15] by the microscopic naïve mode coupling theory (NMCT) [16,17] and the nonlinear Langevin equation (NLE) theory which account for single particle activated barrier hopping [18]. More generally, it is now well established that the full ideal MCT approach [19] is a powerful tool for estimating the onset of transient localization and solidity in diverse colloidal systems [8,19–21]. We do emphasize that though technically much simpler, NMCT captures many of the successes of the full MCT for the system-specific location of the dynamic crossover and localized state properties, is computationally tractable for more complex systems, and serves as the starting point for treating activated dynamics in the NLE approach.

Binary and higher order mixtures are characterized by a much larger parameter space resulting in enhanced property tunability and the possible realization of qualitatively new kinetically arrested states. For example, in so-called biphasic mixtures of equidiameter repulsive and sticky spheres, the attractive species can dynamically arrest in the presence of diffusing repulsive spheres [4], a phenomenon that is qualitatively well described by NMCT and NLE theory [22].

*kschweiz@illinois.edu

Strong asymmetry between mixture species can also be introduced solely via size differences. For example, binary hard sphere fluids exhibit rich collective dynamics that has been extensively studied using simulation [23] and the full ideal MCT [24]. Another interesting feature of mixtures of hard spheres, soft colloids, and polymers and colloids is the influence of structural (e.g., size) asymmetry on the reentrant glass phenomenon [8,9]. The latter is the result of a delicate balance between repulsive-force caging and small-particle mediated physical attraction between the larger species that can effectively refluidize a repulsive glass, and ultimately induce various forms of gelation. In binary asymmetric mixtures, vitrification or gelation can occur simultaneously for both species, or only partially where one component remains an ergodic fluid while the other kinetically arrests. The various MCT approaches have been useful for providing system-specific guidelines for when transient localization and solidlike behavior emerge.

The goal of the present paper is to formulate in general, and apply to the specific system of rods and spheres, a dynamical theory of (ideal) kinetic arrest, shear elasticity, and applied stress-driven yielding of mixtures where at least one of the species is a nonspherical object. Our approach is guided by the previous NMCT of biphasic sphere mixtures [22], and recent work on one-component nonrotating rods [25] and dicolloid suspensions which has been successfully quantitatively confronted with experiment [11,14,15]. Our present focus is solely on constructing ideal kinetic arrest phase diagrams where the boundaries indicate a dynamic crossover from fluidlike behavior to solidlike behavior characterized by transient localization at the center-of-mass level and emergent elasticity, and the effect of applied stress on solidity. For anisotropic particles, the theory is formulated at the simpler center-of-mass (CM) dynamics level [25] corresponding to *dynamically* freezing rotational motion but with the full isotropic fluid structure taken into account. Though seemingly crude, this simplification has been shown to be reliable for the relatively high aspect ratio particles we study [11,14]. Moreover, explicit microscopic treatment of coupled translation-rotation dynamics in glass and gel forming fluids has only been achieved [11–14] for uniaxial shapes due to large technical complexities. Our focus is solely on the local dynamical consequences of conservative forces between objects of finite excluded volume. So-called topological entanglements [26] between highly extended objects (e.g., long rods) are not taken into account. However, these are not expected to be of leading importance in describing the short range physics that underlies isotropic vitrification and physical gelation.

Section II presents the models and dynamical theories employed; technical details of the latter are given in the two Appendices. As relevant background, results for pure rod and pure sphere systems are briefly recalled in Sec. III. Section IV presents the new kinetic arrest phase diagrams and localization parameters predicted for dense rod-sphere mixtures of varying degrees of anisotropy (rod aspect ratio) and interparticle potentials. A few results are also presented as a function of variable total packing fraction. Sample calculations of how the elastic shear modulus and absolute yield stress vary with mixture composition and attraction strength are discussed in Sec. V. The paper concludes in Sec. VI with a brief summary.

II. THEORY

The primary new methodological advance of this article is the generalization of NMCT to treat mixtures where one or more species is a nonspherical object modeled at the interaction site level. Derivation of the self-consistent localization equations, and a microscopic expression for the shear modulus, are given in Appendices A and B, respectively, for a general mixture.

We have recently studied the connectivity percolation of pure (sticky) sphere and rod fluids and their binary mixtures [27]. Here our interest is only high total packing fraction mixtures which are percolated. Hence, whether a gel forms is not limited by connectivity, but rather the formation and lifetime of physical bonds. Here, the latter question is treated only at the simplest NMCT level; generalization to treat the temporal stability of a transiently localized state to activated hopping (bond or cage breaking) events can be achieved using the NLE approach [14,22], but is beyond the scope of this initial work. Thus, a dynamic "phase" exists only in the sense that activated hopping is not allowed, a situation that defines ideal MCT, and is literally relevant in a granular material, and can be practically relevant "deep enough" in the solid-state region of parameter space predicted by MCT.

We model an individual rod as a linearly connected set of spherical interaction sites. Even for rod-sphere mixtures the number of system parameters is large: rod aspect ratio, effective surface corrugation of the rod, rod thickness relative to the sphere diameter, total packing fraction, mixture composition, and the three interparticle site-site potentials. If the latter are described as a hard core plus square well attraction, nine parameters enter: three distances of closest approach, three attraction strengths, and three spatial ranges. Hence, the minimal model has 14 system-specific parameters, and there would be more if additional forces (e.g., Coulomb) were present.

Our approach can address the above level of parameter complexity. But in this initial study we focus on a simpler variant, also relevant to ongoing studies of silver nanowire-nanosphere mixtures by Lewis and co-workers, which we refer to as the "chemically matched" model. Here the interaction sites on the rod have the same hard core diameter as the sphere, d, and the range and strength of the square well attraction (if present) are the same, a and $-\varepsilon < 0$, respectively. The rigid rod is modeled as N tangentially bonded sites corresponding to a fixed bond length between nearest neighbor sites equal to the site hard core diameter. The reduced attraction range $\Delta = a/d$ is fixed at a single small value 0.02 characteristic of nanoparticles or colloids that interact via van der Waals or other short range attractions [1]. We focus on dense mixtures at a total packing fraction of $\eta = 0.4$ unless stated otherwise. Particle volume is quantified based on the hard core diameter, and thus $\eta = \pi d^3(\rho_1 + \rho_2)/6$, where ρ_1 and ρ_2 are the site number densities for spheres and rods respectively. Thus, the number of variable parameters for most cases studied is reduced to three: N, $\Phi_R = \rho_2/(\rho_1 + \rho_2)$, and the contact attraction strength in units of the thermal energy, $\beta\varepsilon$.

A. Particle models and structural correlations

All sites on different particles interact via either a pair decomposable repulsive hard core pair potential or a "sticky" potential consisting of a hard core plus square well attraction:

$$v_s(r) = \begin{cases} \infty, & r < d \\ -\varepsilon, & d < r < d + a \\ 0, & d + a < r. \end{cases} \quad (1)$$

Site-site pair correlation (radial distribution) functions are computed for nonspherical objects using the standard reference interaction site model (RISM) [28–30], or Ornstein-Zernike (OZ) equation [29] for spheres, formulated in terms of a matrix of coupled integral equations which in Fourier space is given by

$$\mathbf{H}(k) = \mathbf{\Omega}(k)\mathbf{C}(k)\left[\mathbf{\Omega}(k) + \mathbf{H}(k)\right]. \quad (2)$$

Here, the matrices $\mathbf{H}(k)$ and $\mathbf{C}(k)$ denote the Fourier transform of $\rho_i \rho_j h_{ij}(r)$ and the direct correlation function $C_{ij}(r)$, respectively, $h_{ij}(r) = g_{ij}(r) - 1$ where $g_{ij}(r)$ is the intermolecular site-site radial distribution function, and $\mathbf{\Omega}(k)$ is a diagonal matrix containing the Fourier transformed intramolecular structure factors $\rho_i \omega_i(k)$ which describes particle shape where ρ_i is the site number density of species i. Subscripts "1" indicate spheres, and "2" indicates rods for which end effects are preaveraged in the standard manner corresponding to an equivalent site approximation [28]. The dimensionless site-site collective partial structure factors are given by

$$S_{ij}(k) = \delta_{ij}\omega_i(k) + \sqrt{\rho_i \rho_j}\, h_{ij}(k). \quad (3)$$

For a sphere, $\omega_1(k) = 1$, while for a tangent bead rod with N sites:

$$\omega_2(k) = \frac{1}{N}\sum_{\kappa, \nu = 1}^{N} \frac{\sin(r_{\kappa\nu}k)}{r_{\kappa\nu}k}, \quad (4)$$

where κ and ν are the site indices on a given rod, and $r_{\kappa\nu} = |\kappa - \nu|d$ is the distance between the two indicated sites. To close Eq. (2) and render it mathematically solvable, the standard site-site Percus-Yevick (PY) approximation [29,30] is employed:

$$\begin{aligned} C_{ij}(r) &= (e^{\beta v(r)} - 1)g_{ij}(r), \quad r > d \\ g_{ij}(r) &= 0, \quad r < d \end{aligned} \quad (5)$$

The coupled integral equations are solved numerically using either the Picard or a Newton-Raphson algorithm [29].

RISM theory predicts the full equilibrium isotropic fluid structure at the site-site, scalar pair correlation function level. It does not capture symmetry-breaking phase transitions such as crystallization or liquid crystal formation [29,30]. This is not a limitation in the present context since our goal is only to study the dynamical arrest of isotropic mixtures. However, RISM theory can predict *isotropic* fluid-fluid phase separation. Of course, for real systems, homogeneous and isotropic glass or gel formation might occur in a metastable sense, for example, in a thermodynamically stable nematic or nonhomogeneous (phase-separated) region of the equilibrium phase diagram. These issues are discussed in Sec. IV.

Concerning the quantitative accuracy of the structural input from RISM theory, it is difficult to make a precise statement. It is well established that RISM theory for the real space site-site pair correlations of dense liquids composed of hard core small molecules is accurate at the 10–20% level [30], but the quantitative accuracy for the sticky rod-sphere mixtures of present interest is not known. For the moderately dense and attractive systems of interest, we suspect it is reasonably accurate, but crisp statements await future equilibrium simulation studies.

B. Naïve mode coupling theory

NMCT is a mathematically and conceptually simplified single particle dynamics version of the full ideal MCT for collective density fluctuations. It has been shown to reliably capture many diverse dynamic crossover phenomena including partial localization in mixtures [22], plastic glasses [14,15], glass-fluid reentrancy [10,31], gel and attractive glass formation [10,14,22,31], nonmonotonic variation with aspect ratio of the arrest volume fraction in fluids of hard uniaxial particles [11,14], and more exotic arrested states in nonspherical particle suspensions [14]. The NMCT arrest boundaries indicate a *crossover* to slow activated dynamics, not the kinetic "glass" or "gel" transition deduced in the laboratory which is based on when a characteristic relaxation time exceeds the experimental time scale. However, many studies have shown deep connections exist between this dynamic crossover and true kinetic arrest [10,14,22,25,31].

The key quantity of NMCT is the long time limit of the CM force-force time correlation function associated with a tagged particle due to interactions with all the surrounding sites on different particles. Within the simplifying CM perspective adopted in this work, rotations are dynamically (*not* statically) frozen. It has been shown that this simplification becomes increasingly accurate as the particle aspect ratio grows beyond ∼1.4 where rotational motion localizes simultaneously with translational motion [14]. Moreover, the nonmonotonic variation of the kinetic arrest boundary with aspect ratio is well captured based on the CM version of NMCT [14]. Note that dynamic freezing only means rotational *motion* is ignored; the full orientationally equilibrated isotropic fluid structure obtained from RISM theory does enter as structural input to NMCT. The CM force-force correlation function is approximately computed using the MCT projection and factorization procedure as outlined in Appendix A. Adopting an Einstein amorphous solid model [16–18] for the kinetically arrested state yields at long times

$$\frac{\beta}{3}\left\langle \mathbf{F}_\alpha^{\mathrm{CM}}(0) \cdot \mathbf{F}_\alpha^{\mathrm{CM}}(t \to \infty) \right\rangle$$

$$= \frac{N_\alpha}{3\beta}\int \frac{d\mathbf{k}}{(2\pi)^3} k^2 \omega_\alpha(k) e^{-k^2 r_{L,\alpha}^2/6}$$

$$\times \sum_{j,k=1}^{2} C_{\alpha i}(k)\sqrt{\rho_i \rho_j}\, S_{ij}(k, t \to \infty)C_{j\alpha}(k), \quad (6)$$

where $\alpha = 1,2$ (sphere, rods), $\mathbf{F}_\alpha^{\mathrm{CM}}(t)$ is the CM force at time t, and the CM localization length is $r_{L,\alpha}^2 = \langle r_\alpha^2(t \to \infty)\rangle$. The *total* force on a tagged molecule due to the surrounding particles, which we refer to as the CM force, is $\mathbf{F}_\alpha^{\mathrm{CM}}(t) \equiv \sum_i^N \mathbf{F}_\alpha^i(t)$, where $\mathbf{F}_\alpha^i(t)$ is the force on site i of a tagged particle of type α.

As discussed in Appendix A, combining Eq. (6) with the CM generalized Langevin equation (GLE) for a mixture leads to the two coupled self-consistent localization equations for the localization lengths

$$\frac{1}{r_{L,\alpha}^2} = \frac{N_\alpha}{9(2\pi)^3} \int d\mathbf{k}\, k^2 \omega_\alpha(k) e^{-k^2 r_{L,\alpha}^2/6} \sum_{j,k=1}^{2} C_{\alpha i}(k)$$
$$\times \sqrt{\rho_i \rho_j}\, S_{ij}(k,t\to\infty)\, C_{j\alpha}(k), \quad \alpha = 1,2. \quad (7)$$

Equation (7) includes two intramolecular structure contributions: $\omega_\alpha(k)$ encodes the *tagged* particle intramolecular site structure, and N_α is the number of sites of a particle of species α. Sites experience *effective* intermolecular pair forces, $\beta^{-1} k C_{\alpha i}(k)$ in Fourier space, due to the surrounding particles. The quantity $e^{-k^2 r_{L,\alpha}^2/6}$ is the single particle Debye-Waller factor, and $S_{ij}(k,t\to\infty)$ is the arrested collective concentration-concentration fluctuation structure factor for species i and j. The latter is determined using a short time Vineyard plus de Gennes narrowing approximation as discussed in great detail in prior work on biphasic sphere mixtures [22]. We refrain from reproducing the lengthy algebraic equations (see Ref. [22]) and only note that $S_{ij}(k,t)$ follows from the exact short time static collective structure factor matrix $\mathbf{S}(k,t)$ of Brownian particles:

$$\frac{d}{dt}\mathbf{S}(k,t) = -k^2 \mathbf{H}(k)\mathbf{S}^{-1}(k)\mathbf{S}(k,t), \quad (8)$$

where $H_{ij}(k) = (k_B T/\zeta_{s,j})\delta_{ij}$ and $\zeta_{s,j} = k_B T/D_{s,j}$ is the short time friction constant for particle type j, and $D_{s,j}$ is the corresponding short time diffusion coefficient. Using $\langle r_\alpha^2(t)\rangle = 6D_{s,\alpha}t$, and taking the long time limit under the assumption particles become localized, leads to the relations $\zeta_{s,j}/\zeta_{s,i} = r_{L,i}^2/r_{L,j}^2$, thereby closing Eq. (7). We emphasize that the arrested collective partial structure factors have both an equilibrium structure contribution ($t = 0$), and a part that depends on the localization lengths of the two species [22].

The emergence of the first $r_{L,\alpha} \neq \infty$ localized solution of Eq. (7) as a function of system parameters signifies the transition from an ergodic fluid to an amorphous solid of species α, which thereby allows the construction of a (ideal) kinetic arrest phase diagram. Within the simplified NMCT, all transitions involve a discontinuous change of the localization length(s), though transitions between different types of arrested states can sometimes be continuous. The nature of the localized state (e.g., glass vs gel) is deduced in NMCT solely from the magnitude of the localization length, or equivalently whether repulsive-force caging or bond formation is the dominant mechanism for arrest. Depending on system parameters, for a binary system three classes of transitions are possible: fluid to double (both species) localized state, fluid to partial (single species) localized state, and single to double localized state.

A microscopic expression for the elastic shear modulus of the ideal solid state has been derived for sphere mixtures [32] using MCT projection and factorization approximations. We have generalized this analysis to mixtures composed of nonspherical particles at the site level. As sketched in Appendix B, the result for a binary mixture is

$$G' = \frac{k_B T}{60\pi^2} \sum_{\alpha,\beta,\gamma,\delta} \sum_{\alpha',\beta',\gamma',\delta'} \int_0^\infty dk\, k^4 \left[\sqrt{\rho_\alpha \rho_\beta}\, \frac{d}{dk} h_{\alpha\beta}(k)\right]$$
$$\times S_{\alpha\delta}^{-1}(k)\left[\sqrt{\rho_{\alpha'}\rho_{\beta'}}\, \frac{d}{dk} h_{\alpha'\beta'}(k)\right] S_{\alpha'\delta'}^{-1}(k) S_{\beta\gamma}^{-1}(k) S_{\beta'\gamma'}^{-1}(k)$$
$$\times S_{\gamma\gamma'}(k,t\to\infty)\, S_{\delta\delta'}(k,t\to\infty). \quad (9)$$

In real systems, thermal fluctuation driven activated hopping can restore ergodicity and fluidize the system on a long enough time scale. Use of Eq. (9) is still appropriate on intermediate time and frequency scales often probed experimentally if the barrier hopping time is sufficiently long. It is in this spirit that we employ Eq. (9) to estimate solid-state rigidity.

C. Nonlinear Langevin equation theory and absolute yielding

NLE theory for one-component spherical and nonspherical particle fluids, and also sphere mixtures, has been developed to go beyond the ideal MCT localization transition to treat ergodicity-restoring single particle activated barrier hopping [14,17,18,22,25]. For binary systems, or translating and rotating molecular fluids, the key idea is a "dynamic free energy surface" that self-consistently quantifies effective forces on a tagged particle within a local equilibrium framework. To construct the dynamic free energy surface, $F_{\mathrm{dyn}}(r_1,r_2)$, for a two-component system one first rewrites Eqs. (6) and (7) in terms of the displacements of tagged species 1 and 2 (r_1 and r_2) as an effective force balance or minimization criterion (to locate a putative localized state) [17,18,22]:

$$\frac{\partial}{\partial r_\alpha} F_{\mathrm{dyn}}(r_1,r_2)\bigg|_{r_{L,\alpha}} = \frac{\beta}{3}\langle \mathbf{F}_\alpha^{\mathrm{CM}}(0)\cdot\mathbf{F}_\alpha^{\mathrm{CM}}(t)\rangle_{r_{L,\alpha}} - 3k_B T/r_{L,\alpha}$$
$$= 0. \quad (10)$$

The corresponding coupled NLE equations then follow in the overdamped limit as [18,22]

$$-\zeta_{s,\alpha}\frac{d}{dt}r_\alpha - \frac{\partial}{\partial r_\alpha}F_{\mathrm{dyn}}(r_1,r_2) + \delta f_\alpha = 0, \quad \alpha = 1,2,$$
$$\langle \delta f_\alpha(0)\delta f_\gamma(t)\rangle = 2k_B T \zeta_{s,\alpha}\delta_{\alpha\gamma}\delta(t), \quad (11)$$

where r_α is a dynamic scalar displacement and δf_α is a fluctuating force felt by a tagged particle of type α related by the fluctuation dissipation theorem to the dissipative drag force quantified by a short time friction constant. Equation (11) is constructed such that if the noise term is dropped, and hence systems cannot go "uphill" over a barrier, the NMCT self-consistency relations of Eq. (7) are obtained for the ensemble-averaged localization lengths in the long time limit.

As discussed in great detail previously [14,25,33], the effect of applied stress (σ) is modeled in a simple scalar microrheology framework as an external force on tagged particles deduced from the macroscopic stress and an estimate of the average particle cross sectional area. Equation (10) is thus modified with an additional microscopic external force

term as

$$\left.\frac{\partial}{\partial r_\alpha} F_{\text{dyn}}(r_1, r_2)\right|_{r_{L,\alpha}} = \frac{\beta}{3}\left\langle \mathbf{F}_\alpha^{\text{CM}}(0)\cdot\mathbf{F}_\alpha^{\text{CM}}(t)\right\rangle r_{L,\alpha}$$
$$- 3k_B T / r_{L,\alpha} - f_\alpha^{\text{micro}} = 0, \quad \alpha = 1, 2,$$

(12)

where $f_\alpha^{\text{micro}} = \lambda(N_\alpha d^2 \sigma / \eta^{2/3})$ is the additional microscopic force, σ is in units of $k_B T / d^3$, and λ is a numerical coefficient of order unity of geometric origin that is not predicted from first principles. Depending on the average particle cross section employed to relate the macroscopic stress and microscopic force, λ varies slightly [33]. Here, we set $\lambda = 1$ without loss of generality since all results for stress can be scaled appropriately for $\lambda \neq 1$.

Beyond a so-called "absolute" yield stress σ_y, the localized state predicted by quiescent NMCT is by definition destroyed. Within the NLE perspective, this corresponds to when the activation barrier goes to zero, or equivalently when the external force becomes equal and opposite to the maximum intermolecular force confining particles to a localized state. This absolute yield stress is directly relevant for understanding a mechanically driven solid-to-fluid transition in granular systems where thermal fluctuation induced barrier hopping is not present. For thermal Brownian suspensions or liquids, it represents an upper bound to an experimentally relevant "dynamical" yield stress which qualitatively signals when the stress-assisted mean barrier hopping time is of order of the observation time scale [1,14,33,34]. In practice, we determine the absolute yield stress using a bisection technique to find the value of $\sigma = \sigma_y$ that removes all finite $r_{L,\alpha}$ solutions to Eq. (12). The possibility for multistep yielding (sequential destruction at distinct stresses of a doubly localized state [14,34]) exists; however, our initial studies in this paper only explore absolute yielding.

The extension of NMCT to include applied deformation is simple and largely heuristic. However, it is motivated by both recent and old physical concepts, including the Eyring idea that applied stress speeds up dynamics, and the modern microrheology perspective of relating macroscopic stress to an effective force on a tagged particle level [33]. Our treatment ignores all tensorial aspects of the deformation (e.g., shear versus extension) given our desire to describe tagged particle motion in an isotropic (spherically averaged) manner. The adopted simplicity allows one to avoid having to know vectorial measures of anisotropic structure, a very difficult problem. Indeed, various experimental and simulation studies often find little changes of isotropic local structure even at high stresses or strains where the dynamics is changed by orders of magnitude (see [33] for a discussion), an implicit assumption of our present analysis. Finally, the usefulness of our simplified isotropic perspective is supported by prior successful applications of the stressed versions of NMCT and NLE to diverse experimental colloid phenomena, especially mechanically induced yielding [14,33,34].

III. PURE SPHERE AND ROD FLUIDS

As relevant background, a qualitative, but faithful depiction of a typical one-component NMCT and NLE kinetic arrest
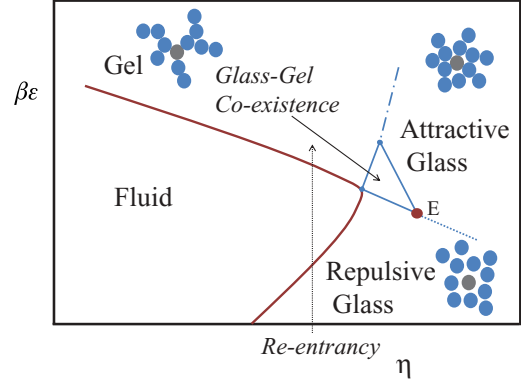

FIG. 1. (Color online) A qualitatively correct schematic of the ideal kinetic arrest diagram for one-component liquids of spheres or rods at the CM level as predicted by NMCT and NLE theory [10]. Distinct dynamically arrested states are gels, attractive glasses, repulsive glasses, and the glass-gel coexistence regime. The E point defined within the NMCT framework signals only the termination of the ability to distinguish repulsive and attractive glasses based on their localization length [6–10]. The dashed line beyond the E point is a fuzzier crossover boundary indicating a rapid, but smooth, change from glasslike to gel-like localization [10]. The heavy solid curve surrounding the fluid regime indicates the initial fluid-to-solid ideal transition or dynamic crossover. Sketches of particle arrangements in various states are shown. The reentrancy arrow indicates a sample trajectory for a repulsive glass → fluid → gel transition.

diagram for attractive spheres is shown in Fig. 1 [8,10]; the topology is qualitatively the same for rods [14,25] and other shapes at the CM level [10]. Four distinct (ideal) dynamically arrested states are predicted [6–10]: repulsive glass (RG), gel (G), attractive glass (AG), and a glass-gel co-existence (GGC) region. RG and G states are distinguished in NMCT by the value of the localization length; specifically, a repulsive glass has a relatively large localization length since arrest is driven by caging forces, while gels exhibit a shorter localization length tightly correlated with the (short) range of the attractive interaction that induces physical bond formation. The AG and GGC are identified based on the form of the dynamic free energy [10]. Attractive glasses are characterized by gel-like localization lengths but dynamical barriers at (larger) glasslike displacements; the GGC state corresponds to a narrow regime of parameter space where the dynamic free energy exhibits two localization wells and two (low) barriers. The nonmonotonic "nose" feature in Fig. 1 signals a reentrancy transition from RG → fluid (F) → G or AG associated with a change from repulsive-force caging to attractive force bond formation as the primary mechanism for transient localization [6–10].

Ideal dynamic arrest phase diagrams for the pure component fluids are presented in Fig. 2; above (below) the curves indicate an arrested solid (ergodic fluid). Only the initial nonergodicity boundary is presented (not the dashed lines corresponding to continuous, but rapid, changes of the localization length, nor the E point in Fig. 1) which is the focus of our present work. As one transitions from spheres to $N = 5$ rods to $N = 40$ rods, the fluid regime shrinks dramatically. Easier dynamical arrest at higher aspect ratios is an intuitive result of increased particle anisotropy which magnifies both steric excluded volume constraints and the
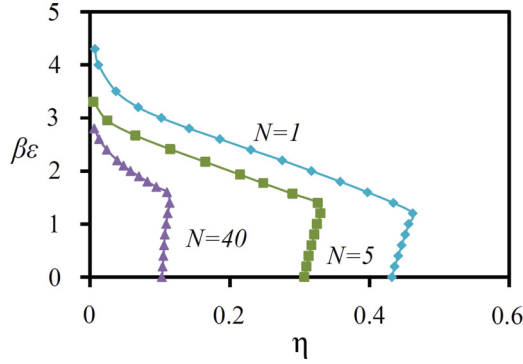
FIG. 2. (Color online) NMCT dynamic crossover boundaries for a reduced attraction range of $\Delta = 0.02$ of (top to bottom): pure spheres (teal diamonds), five site rods (green squares), and 40 site rods (purple triangles). The glass-gel coexistence regime, E point, continuous transitions from the gel to attractive glass, and the repulsive glass to attractive glass transition are not shown. Only the initial nonergodicity boundary is presented, which is the focus of our present work.

ability to form intermolecular physical bonds. We note that NMCT only predicts local stability of the arrested state to small amplitude Gaussian-like dynamic fluctuations. Neither large amplitude activated barrier hopping nor the question of whether a gel is bond percolated are addressed. For a space spanning kinetically stable gel to exist, one intuitively expects the minimum requirements are that the physical bonds have a lifetime longer than the experimental time scale, and the system is geometrically bond percolated. These issues were discussed in our prior work that studied single-component sphere and rod suspensions and bond percolation of rod-sphere mixtures [27]. Since our present interest is dense mixtures, the percolation criterion is obeyed. In all calculations presented below the parameter ranges studied correspond to homogeneous states, i.e., liquid-liquid demixing does not occur.

IV. DYNAMICAL ARREST PHASE DIAGRAMS AND LOCALIZATION LENGTHS OF ROD-SPHERE MIXTURES

A. Five site attractive rods with attractive and hard spheres

We first study a binary mixture of $N = 5$ rods and hard spheres where attractions are present only between rod sites. The results are shown in Fig. 3, and demonstrate this binary mixture is significantly more complex than a one-component suspension. Multiple dynamic "triple points" and reentrancies are predicted. There is a large fluid regime along with three distinct arrested states. Starting in the fluid window and increasing the interrod attraction strength results in physical bond formation and gelation of only the relatively dilute rod species. Hence, this gel is porous and the spheres remain liquidlike, i.e., delocalized. At higher rod composition the gel pore size shrinks and the spheres eventually become trapped in a glassy state via steric excluded volume constraints. Consequently, a new arrested state with both gel and glass characteristics [10] is predicted. Another notable feature is the double glass reentrancy in Fig. 3, which qualitatively is a consequence of the same competing physics operative in sticky single-component fluids: attractions cause physical clustering thereby creating
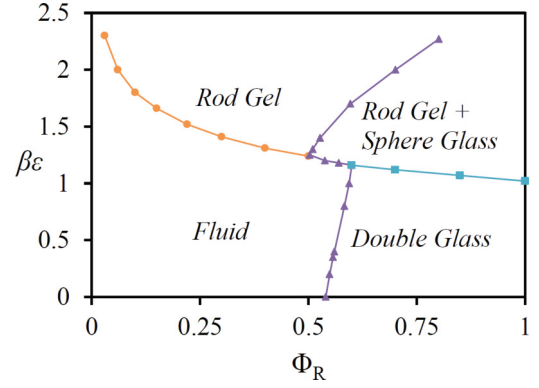

FIG. 3. (Color online) Ideal kinetic arrest phase diagram for a binary mixture of $N = 5$ site attractive rods and hard spheres at $\eta = 0.4$. Orange spheres signify the appearance of a rod gel, purple triangles the onset of double (rod and sphere) localization, and the teal squares a discontinuous change from a double glass (where rods and spheres have relatively large localization lengths) to a sphere glass and rod gel which has a smaller localization length.

more "free volume" at intermediate levels of attraction strength [6–10]. Over a narrow range of rod compositions near $\eta = 0.5$, a vertical trajectory can involve three kinetic transitions: double glass → fluid → rod gel plus sphere glass → rod gel. At very high rod loadings, increasing rod attraction results in a double glass → rod gel plus sphere glass transition; further increase of attraction leads to another type of reentrant melting whence the rods are gels but the spheres refluidize.

The boundaries separating the various regimes in Fig. 3 are determined from the computed jump discontinuities in one or both of the localization lengths. Figure 4 plots the localization lengths along three trajectories in the dynamic phase diagram of Fig. 3. The vertical trajectory at $\Phi_R = 0.57$ illustrates the influence of reentrancy on the localization lengths. At low $\beta\varepsilon$, both rods and spheres are glassy with relatively large localization lengths ($\sim 0.10d$), though the rod r_L is smaller due to its larger steric hindrance. One physically expects (confirmed in Sec. V) that these localization lengths
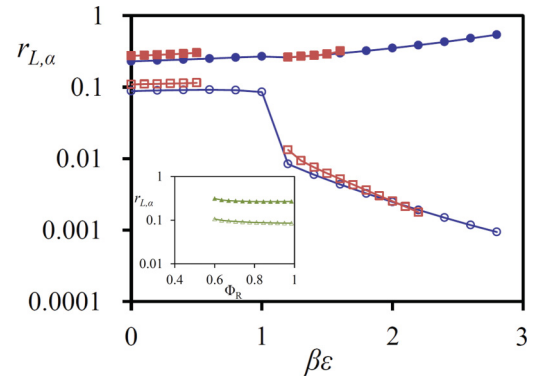

FIG. 4. (Color online) Localization lengths (units of site diameter) along different trajectories in Fig. 3: at constant Φ_R in the main plot, and at constant $\beta\varepsilon$ in the inset, at fixed $\eta = 0.4$. Solid and open red squares represent spheres and rods, respectively, at $\Phi_R = 0.57$. Solid and open blue circles in the main figure represent spheres and rods, respectively, for $\Phi_R = 1$. Inset: Solid and open green triangles represent spheres and rods, respectively, at $\beta\varepsilon = 1$.

correlate with shear rigidity: the smaller r_L, the greater the shear modulus. At large $\beta\varepsilon$, the double glass melts and an ergodic fluid is predicted. Further increase in the rod attraction resolidifies the system with spheres in a glassy state and rods in a gel state as deduced by the abrupt decrease of the rod localization length.

A strong similarity of the rod localization lengths of the $\Phi_R = 1$ and $\Phi_R = 0.57$ systems is also seen in Fig. 4. However, for the pure rod fluid, increasing rod attraction does not liquefy the mixture. Upon crossing $\beta\varepsilon \sim 1$, a change from a double glass to a rod gel plus sphere glass state is predicted. This crossover results in an increase in the sphere localization length, a seemingly counterintuitive change that occurs since enhanced rod physical bonding results in additional free volume for the hard spheres. Localization length results along a horizontal $\beta\varepsilon = 1$ trajectory in Fig. 3 are also presented in Fig. 4. Below $\sim$60% rods the mixture is a fluid, while above this threshold a double glass emerges, and further increase of the rod composition has little influence on the localization lengths of either species.

Figure 5 shows the analogous kinetic arrest map when the spheres now attract each other and also the rods with exactly the *same* strength as the interrod site-site attraction. Differences in static structure between the fully attractive and mixed hard-attractive system, discussed previously [27], result in new features of kinetic arrest, though some aspects of Fig. 3 persist. Sphere attractions allow for their active participation in the physically bonded network which greatly reduces the rod gel window. Additionally, the rod gel-sphere glass regime is nearly erased. Multiple dynamic "triple points" and reentrancies are again predicted. Note that rather large colocalized double gel and double glass regimes are present, accompanied by small single rod gel and mixed sphere glass-rod gel regimes. These features are presumably a consequence of the relatively low rod aspect ratio and modest mixture structural packing asymmetry. The double gelation boundary in Fig. 5 is surprisingly flat and slowly varying with mixture composition. It is not immediately obvious why such
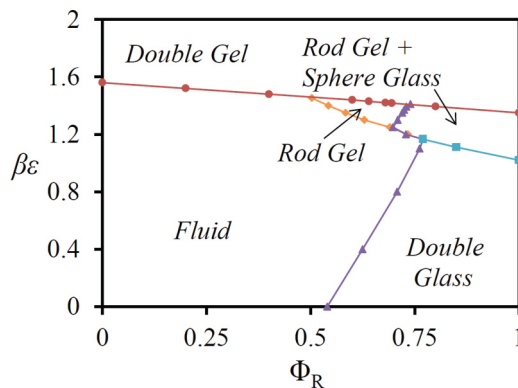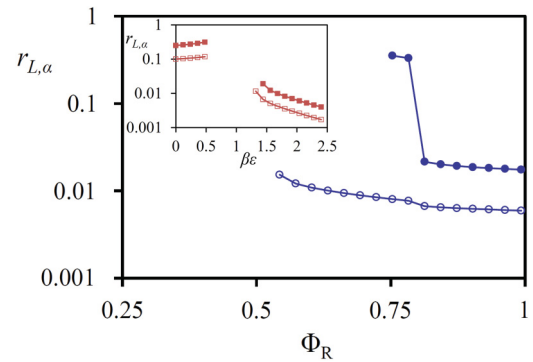

FIG. 6. (Color online) Localization lengths (units of site diameter) along trajectories in Fig. 5: at constant $\beta\varepsilon$ in the main plot, and at constant Φ_R in the inset, at fixed $\eta = 0.4$. Solid and open blue spheres in the main figure represent spheres and rods, respectively, for $\beta\varepsilon = 1.4$. Inset: Solid and open red squares represent spheres and rods, respectively, at $\Phi_R = 0.66$.

large insensitivity to composition should exist, but recall the "chemistry" is matched in the studied model. This suggests physical bonding requires a minimum attraction between sites that is largely independent of intramolecular architecture, as perhaps expected given the very short range attractive force.

Comparing Figs. 3 and 5 also demonstrates the large influence of sphere-sphere attraction on dynamic reentrant melting. Specifically, it strongly enhances the reentrant noselike feature encapsulating the fluid regime. Stronger reentrancy results from enhanced particle clustering as spheres can also form physical bonds thereby opening up even more "free volume."

Figure 6 shows the localization lengths corresponding to two sample trajectories in the double localized regime of Fig. 5. Following the horizontal $\beta\varepsilon = 1.4$ trajectory with increasing Φ_R highlights the numerous dynamical state changes possible: the rods and spheres are initially fluid, then the rods gel, followed by sphere glass formation in the rod gel, and finally double gelation. When spheres localize into a glassy state little influence is predicted on the rod localization length, in contrast to sphere gelation which induces a noticeable change in the rod localization length due to the increase in particles participating in physical bonding and hence tighter clustering. Lastly, the vertical trajectory along $\Phi_R = 0.66$ in Fig. 6 (inset) exhibits the familiar reentrancy phenomenon in mixtures. Transitions from a double glass $\rightarrow$ fluid $\rightarrow$ rod gel $\rightarrow$ double gel are predicted, along with striking changes in the localization lengths.

Overall, upon mixing modest length rods and spheres, especially if both are sticky, results in a remarkable increase in complexity of the kinetic arrest diagram. New confocal imaging experiments are in progress by Lewis and co-workers to probe these kinetic arrest and localization length predictions for dense mixtures of sticky silica rods and repulsive or attractive spheres.

FIG. 5. (Color online) Ideal kinetic arrest phase diagram for a binary mixture of $N = 5$ site attractive rods with sticky spheres at $\eta = 0.4$. Orange diamonds denote the appearance of a rod gel (in a background ergodic sphere fluid), purple triangles the onset of double localization, teal squares a discontinuous change from a double glass with relatively large localization lengths to a rod gel plus sphere glass state, and red circles indicate a discontinuous transition to a double gel.

B. 40 site attractive rods with attractive and hard spheres

Before presenting our results for binary fluids involving $N = 40$ rods, a possible complication must be discussed: nematic liquid crystal formation and orientational packing correlations for high rod aspect ratios and/or concentrations.

As mentioned earlier, most standard integral equation approaches (including RISM-PY) are not capable of predicting nematic phase formation [28–30]. However, whether such an equilibrium phase transition is relevant for nonequilibrium glass or gel formation is not *a priori* obvious. This issue is analogous to the relation between crystallization and vitrification in spherical particle systems. Here, the crystalline states are often irrelevant for practical reasons, e.g., size polydispersity and/or slow nucleation kinetics. As a result it is the equilibrated metastable amorphous branch for spheres that is relevant. In analogy, for rodlike objects the formation of *isotropic* rod gels or glasses is very common in synthetic and biological systems [3], despite the equilibrium driving force to form nematics. Thus, homogeneous isotropic rod gels are possible as long as kinetic arrest preempts long range orientational ordering, which is the scenario assumed in the calculations presented below. A second possible complication is that, even in the isotropic phase, one expects spatially short range orientational correlations between rods are present. The standard RISM-PY theory we employ does not capture this aspect [30]. However, note that such vectorial correlations do not enter the dynamical NMCT theory for particles described by an interaction site model.

Figure 7 shows that large rod anisotropy leads to striking new features in the dynamic phase diagram of fully attractive rod-sphere mixtures. A total of seven dynamically arrested "phases," multiple dynamic triple points, and many reentrant features are predicted. The fluid regime is now very small, and the rods are localized over a much greater portion of parameter space than when $N = 5$. Rods can form a single gel, single glass, or single attractive glass in the presence of a sticky sphere fluid. Additionally, the theory predicts a single rod glass-gel coexistence regime. Overall, the structure of the single rod dynamic crossover boundaries in Fig. 7 is similar to a representative one-component rod analog in Fig. 2.

Increasing rod length from $N = 5$ (Fig. 5) to $N = 40$ (Fig. 7) is also predicted to result in little change of the doubly
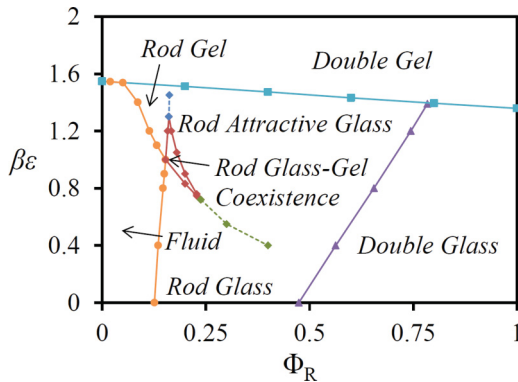
FIG. 8. (Color online) Localization lengths (in site diameter units) along trajectories in Fig. 7 at constant Φ_R with $\eta = 0.4$. Solid and open blue spheres represent spheres and rods, respectively, for $\Phi_R = 0.153$. Solid and open red squares represent spheres and rods, respectively, at $\Phi_R = 0.3$.

arrested boundaries. Qualitatively, and even quantitatively for double gelation, the kinetic arrest boundaries are the same for $N = 5$ and $N = 40$ site rods. This insensitivity may be due to the spheres not "seeing" the full rod length but rather a dense intertwined network or mesh of rods. In contrast to the $N = 5$ rod mixtures, when $N = 40$ there is a rather wide separation of the kinetic arrest boundaries of rods and spheres in the dynamic phase diagram. Effectively, the kinetic arrest map bifurcates into (1) a region of localized rods in a background sphere fluid, and (2) well removed doubly arrested states. As we shall see, this has major consequences on mechanical properties such as the elastic modulus and yield stress.

Localization length calculations along two trajectories in Fig. 7 are shown in Fig. 8. Along the vertical $\Phi_R = 0.153$ trajectory the inner corner of the glass-gel coexistence regime is traversed. Dynamic transitions from a rod glass → rod gel → double gel are predicted. Following the $\Phi_R = 0.3$ trajectory similar changes of the localization lengths are found. However, a *continuous* (smooth crossover) transition from a rod repulsive glass to a rod attractive glass is observed; recall these two states are distinguished by inspection of the corresponding scalar dynamic free energy as explained previously [10]. When the spheres do gel in Fig. 8 for both the $\Phi_R = 0.153$ and $\Phi_R = 0.3$ trajectories, the rod r_L drops much more dramatically than found for the $N = 5$ rod phase diagrams. Upon sphere gelation, a transition from <40% to 100% of the particles forming physical bonds occurs. The pronounced change in the number of bonding particles produces the large discontinuous drop in the rod localization lengths.

Finally, we examine $N = 40$ site attractive rods mixed with hard spheres in Fig. 9. At a gross level the overall topology of Figs. 7 and 9 is the same, except for the lack of a double gel in the hard sphere case. This results in a large "hole" in the middle of the phase diagram where rod glasses in an ergodic sphere fluid exist. The shape of the double glass boundary also qualitatively changes. One additional subtle difference is the disappearance of the single rod reentrant feature, in contrast to the $N = 5$ rod mixture behavior in Figs. 3 and 5. We interpret this as a consequence of the large separation of the single rod localization and double localization boundaries. If sphere attractions are absent, then any additional free volume gained

FIG. 7. (Color online) Ideal kinetic arrest phase diagram for a binary mixture of $N = 40$ site attractive rods with sticky spheres at $\eta = 0.4$. Orange circles denote the appearance of a rod glass or gel (in a background ergodic sphere fluid), purple triangles the onset of double glass formation, teal squares a discontinuous transition to a double gel, and red diamonds indicate the glass-gel coexistence boundary. The dashed blue diamonds (rod gel to rod attractive glass) and dashed green diamonds (rod repulsive glass to rod attractive glass) represent continuous changes in the localization length parameters [10].
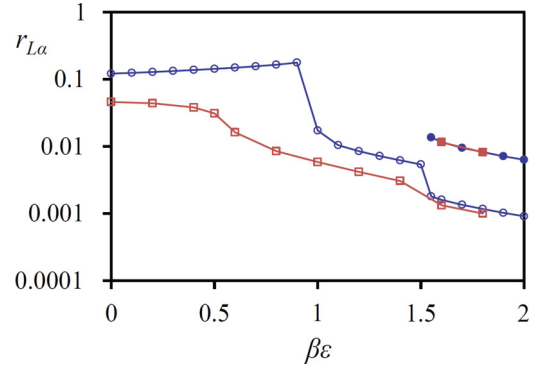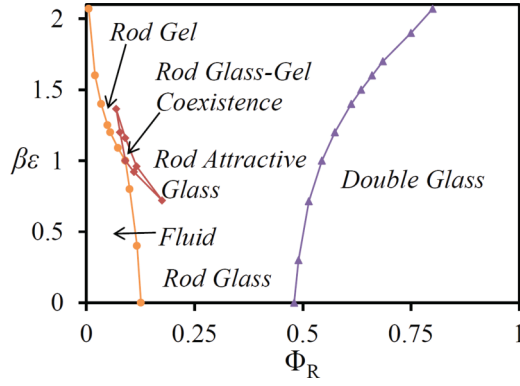
FIG. 9. (Color online) Ideal kinetic arrest phase diagram for a binary mixture of $N = 40$ site attractive rods with hard spheres at fixed $\eta = 0.4$. Orange circles denote the onset of rod localization (in an ergodic sphere fluid), purple triangles the onset of double glass localization, and red diamonds the glass-gel coexistence boundary.

by their aggregation is removed since spheres now repel, not stick.

C. Dynamic phase diagrams in the η-Φ_R plane

Dynamic phase diagrams in the η-Φ_R plane probe another aspect of parameter space associated with the total mixture packing fraction. Figure 10 shows an example for an athermal mixture of hard spheres and five site *hard* rods; note the relevant total packing fractions are still quite high. The fluid window is very large, and the onset of localization occurs simultaneously for both species in the majority of parameter space. Only a small regime at high rod composition exists where rods localize but spheres remain fluid. Rods can arrest in the presence of a sphere fluid via a combination of anisotropy and porosity; when the latter decreases enough with increased rod loading the spheres become trapped in the small pores of the rod glass. The difference between the kinetic arrest packing fraction of spheres and rods grows with Φ_R.

It is interesting to compare the onset point when rods localize but the spheres do not (dynamic "triple point" Z in Fig. 10) to the onset volume fraction in the pure five site rods of Fig. 2. The rod packing fraction at point Z is
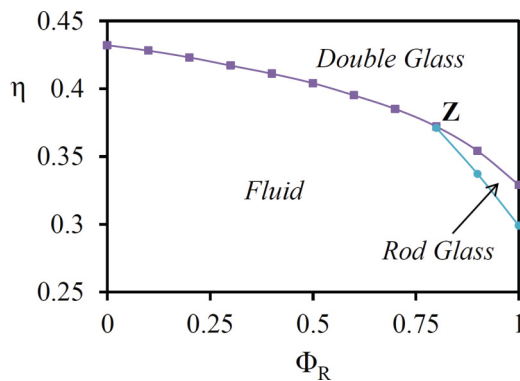

FIG. 10. (Color online) Ideal kinetic arrest phase diagram for a binary athermal mixture of $N = 5$ site hard rods with hard spheres in the representation of total mixture packing fraction versus rod volume fraction.
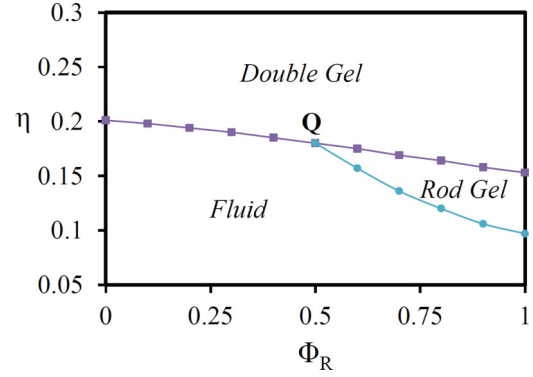

FIG. 11. (Color online) Ideal kinetic arrest phase diagram for a binary mixture of $N = 5$ site attractive rods and attractive spheres (common value of $\beta\varepsilon = 2$) in the representation of total mixture packing fraction versus rod volume fraction.

$\eta_{\rm eff} = \eta \times \Phi_R = 0.3$, which is nearly identical to the pure hard rod crossover at $\eta = 0.31$ in Fig. 2. This small difference suggests calculations for pure component systems can be useful for predicting the onset of single dynamical arrest in rod-sphere mixtures, even if the elementary excluded volume scales (d) are identical.

The role of rod attractions in the η-Φ_R kinetic arrest diagram is studied in Fig. 11 at a fixed (rather strong) $\varepsilon = 2k_B T$. As expected, attractions greatly reduce the fluid window compared to the hard rod mixture of Fig. 10. Additionally, there are no glassy regimes, only gel states. Colocalization now occurs only over roughly half the range of mixture compositions, much less than in Fig. 10. The large double gel window arises from clustering and bond formation between all species. Comparing the dynamical triple point Q in Fig. 11 to the pure component analog in Fig. 2, one sees that $\eta_{\rm eff} = 0.09$ and $\eta = 0.103$. Again, a rather good agreement between the two quantities is found. We do caution that the generality of such agreement is unclear since the models studied here have matched chemistry and elementary (site-level) excluded volume scales which results in weak structural or packing variations in the mixture. The latter holding with varying composition may be key to realizing reliable predictive ability for effective one-component descriptions.

We note that the full ideal MCT of collective pair dynamics has been employed to study kinetic arrest of hard *sphere* mixtures characterized by diameter (D) asymmetries ($\delta = D_{\rm small}/D_{\rm large}$) ranging from $\delta = 0.5$ to 0.8 [24]. In all cases, the ideal glass transition total volume fraction boundaries are nonmonotonic functions of composition, in contrast to our results in Fig. 10. We interpret this difference as indicating rods cannot be viewed as simply larger spheres, and explicit rod anisotropy plays a crucial dynamical role.

V. ELASTIC MODULUS AND ABSOLUTE YIELD STRESS

Crossing the dynamic arrest boundaries in Figs. 3, 5, 7, and 9–11 can lead to dramatic changes of bulk mechanical properties. For one-component systems, there is a direct correlation between the shear modulus and the inverse localization length within NMCT [10,33,35]. A mixture is more complicated, and the relative contribution of different species to elasticity is an
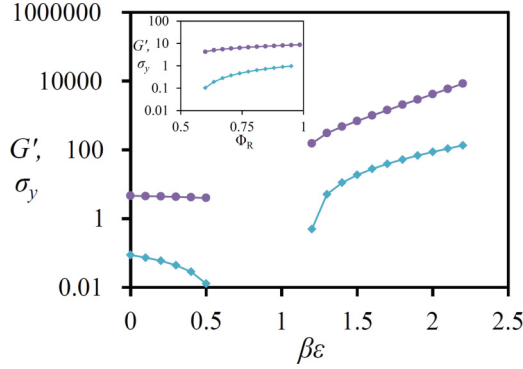
FIG. 12. (Color online) Mechanical properties (units of $k_B T/d^3$) of a mixture of $N = 5$ site attractive rods and hard spheres corresponding to Figs. 3 and 4. The purple circles (upper) and teal diamonds (lower) indicate G' and σ_y, respectively. The main figure is at a constant rod composition of $\Phi_R = 0.57$, and the inset is at constant $\beta\varepsilon = 1$.

issue. But qualitatively, the connection between higher rigidity and tighter localization is physically expected. In this section we present sample calculations of how the shear modulus G' and absolute yield stress σ_y vary along specific trajectories in the kinetic arrest diagram. We define an "absolute yield strain" as the ratio $\gamma_y \equiv \sigma_y/G'$, the value of which is a measure of the "brittleness" of an amorphous solid.

For the mixture of hard spheres and $N = 5$ attractive rods in Fig. 3, calculations of the dimensionless G' and σ_y at $\Phi_R = 0.57$ as a function of attraction strength are presented in Fig. 12; the corresponding localization lengths were shown in Fig. 4. The units are $k_B T/d^3$; at room temperature, this corresponds to 4200, 4.2, and 0.0042 Pa for a site diameter of 10, 100, and 1000 nm, respectively. Both the shear modulus and absolute yield stress are small at low $\beta\varepsilon$ where the mixture is a double repulsive glass. Increasing $\beta\varepsilon$ leads to reentrancy (double glass melts into a fluid) and the vanishing of G' and σ_y. Further increase of rod attraction results in the reemergence of a nonzero yield stress and elastic modulus due to double gelation. In the gel state, both G' and σ_y are $\sim$1–3 orders of magnitude larger (increasing roughly exponentially with reduced attraction strength) than in the glass due to the presence of strong bonds and very tight particle localization. Yield strains are small, well below 10%, and often $\sim$1%, implying brittle gels. This behavior is intimately related to the fact that gel rigidity arises from the formation of very tight physical bonds which induce much more particle localization than in repulsive-force controlled glasses stabilized by particle caging.

To illustrate the effect of mixture composition on mechanical properties, a horizontal trajectory at fixed $\beta\varepsilon = 1$ in Fig. 3 is shown in the inset of Fig. 12. Both G' and σ_y monotonically increase with rod composition, implying rods are more effective at storing stress and impart greater rigidity than spheres even at fixed total packing fraction. For this glassy mixture, the yield stress is a more strongly increasing function of rod composition, implying a higher yield strain. Based on many other calculations, we conclude particle shape anisotropy enhances both caging and bond formation in all arrested states and thus increases both the linear elastic modulus and the absolute yield stress.

To elaborate further on the physical interpretation of the above results, we recall that in one-component systems the elastic modulus is related to the inverse of the localization length in the context of NMCT as

$$G' \approx \frac{9\eta k_B T}{5\pi d r_L^2}. \tag{13}$$

This result has been analytically derived from an ultralocal limit analysis [35] of Eq. (9) for one-component arrested solids, and verified numerically (and via experiment for depletion and other particle gels [36]) based on many NMCT studies of glasses and gels of both spherical and nonspherical particles [10,25,31,33]. To the extent that yield strains are not very variable, one expects yield stresses and the linear modulus to be tightly correlated with regard to their response to system parameters and thermodynamic state. While lacking a more rigorous foundation for mixtures, we physically expect a relation such as Eq. (13) still applies. Support for this statement is provided by comparing Fig. 12 to the corresponding Fig. 4. Whenever the localization lengths decrease, G' and σ_y grow. Note that near the onset of the localized state, the shear modulus and absolute yield stress do vary in a significantly different manner. The reason is that G' is discontinuous since a finite localization length emerges abruptly, but the absolute yield stress is directly proportional to the maximum restoring force localizing a particle which becomes nonzero in a continuous fashion [33,35]. Hence, σ_y changes in a smooth, albeit steep, manner upon transition from the liquid to solid state. Note that in Figs. 12 and 13 the continuous nature of the absolute yield stress at melting is obscured because of the logarithmic scale and point spacing/resolution used.

Figure 13 shows mechanical property results for the fully attractive $N = 5$ rod mixture at fixed $\beta\varepsilon = 1.4$ corresponding to a horizontal trajectory in Fig. 5. This mixture is a fluid at low enough Φ_R, but upon crossing the rod gel boundary, a large G' and σ_y emerges. Further increase in rod composition results in the formation of a double gel, and at this boundary the shear modulus and yield stress increase discontinuously (but weakly) due to the sudden added sphere contribution to elasticity. The very weak discontinuity again emphasizes the
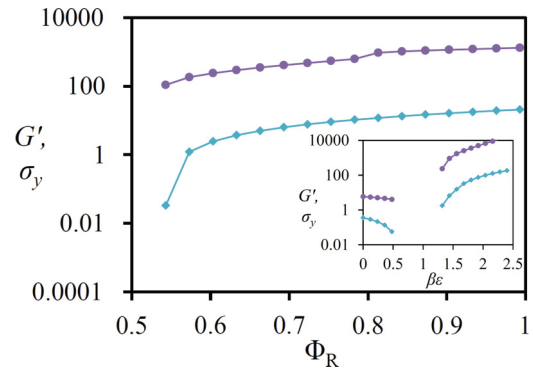

FIG. 13. (Color online) Mechanical properties (units of $k_B T/d^3$) of a mixture of $N = 5$ site attractive rods with attractive spheres corresponding to Figs. 5 and 6. The purple circles (upper) and teal diamonds (lower) indicate G' and σ_y, respectively. The main figure is at constant $\beta\varepsilon = 1.4$, and the inset at a constant rod composition of $\Phi_R = 0.66$.
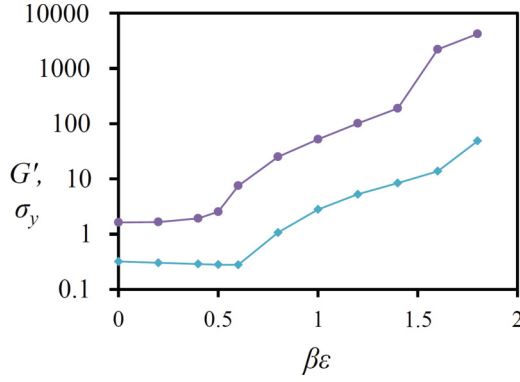
FIG. 14. (Color online) Mechanical properties (units of $k_B T/d^3$) of a mixture of $N = 40$ site attractive rods with attractive spheres corresponding to Figs. 7 and 8. The purple circles (upper) and teal diamonds (lower) indicate G' and σ_y, respectively, at $\Phi_R = 0.3$.

dominant role played by the rods in conferring rigidity to the mixture. The yield strain in all cases is of order 1%, which is characteristic of a brittle rod gel. The inset shows results along a $\Phi_R = 0.66$ vertical trajectory. This provides an example where reentrancy is present in the mixture. Behaviors similar to the analogous trajectory in Fig. 12 are found. Additionally, the mechanical properties in Fig. 13 can be compared to the analogous localization lengths in Fig. 6, and their correlation is very similar to the $N = 5$ rod systems.

One final example is presented in Fig. 14 for the fully attractive $N = 40$ rod mixture at $\Phi_R = 0.3$. With increasing composition the system changes from a rod glass $\rightarrow$ attractive glass $\rightarrow$ double gel. Many decades of change in the rigidity are predicted, and the three regimes all exhibit different sensitivities to attraction strength, with the attractive gel being most responsive. This trend is consistent with the more brittle nature of gel-like localized states compared to repulsive glasses. In Fig. 14, below $\beta \varepsilon \sim 0.5$ the system is a rod glass with a nearly constant yield stress of $\sigma_y \sim 0.20$. Upon increasing the attraction further, there is a smooth transition from a rod glass to a rod gel with an accompanying increase of the yield stress to much higher values. When the double gel boundary is crossed at $\beta \varepsilon \sim 1.5$, the spheres add to the elasticity and the yield stress is further enhanced. In the double gel state the rods and spheres are all tightly bonded so very small deformations are sufficient to fluidize the material.

While not explicitly presented here, Eq. (9) can be decomposed [22] into components from rod-rod, rod-sphere, and sphere-sphere correlations associated with the three distinct contributions to the total stress-stress autocorrelation function (see Appendix B). Rod-rod contributions arise from all terms in the sums of Eq. (9) with $\partial_k h_{rr}(k) \partial_k h_{rr}(k)$, sphere-sphere contributions from $\partial_k h_{ss}(k) \partial_k h_{ss}(k)$, and everything else defines the rod-sphere cross contributions. Using this separation, one can define $G' \equiv G'_{rr} + G'_{rs} + G'_{ss}$. For $N = 40$ rod mixtures at compositions greater than $\sim$40% the dominant contribution to the mixture elastic modulus is from the rods. On the other hand, for the shorter $N = 5$ mixture, rod compositions must exceed $\sim$49% for the latter situation to hold, and even here spheres store a comparable amount of stress as do the rods. The difference between $N = 5$ and $N = 40$ attests to the ability of

particle shape anisotropy to aid in dynamic arrest and provide higher rigidity.

VI. CONCLUDING REMARKS

We have extended the quiescent and stressed versions of NMCT and NLE theory to treat the kinetic arrest, elastic modulus, and absolute yielding of particle mixtures with one or more species of dynamically nonrotating, nonspherical objects described at the center-of-mass translation level. The theory has been applied in detail to dense isotropic mixtures of variable aspect ratio rods and spheres that interact via repulsive and/or short range attractive site-site pair potentials. For simplicity, a "chemically matched" model was studied corresponding to equal diameter of the spheres and rod interaction sites, and (when present for all species) matched attraction strength and range. Even given this reduction of system parameters, the predicted kinetic arrest behavior is remarkably rich. Up to eight "dynamical phases" can emerge that fall into four distinct categories: (i) ergodic fluid, (ii) partially localized states where the spheres remain fluid but the rods can be in gel, repulsive glass, or attractive glass states, (iii) doubly localized glasses, gels, or a porous rod gel plus sphere glass, and (iv) a very narrow window for long rods where single glass and single gel type localization coexist. Multiple dynamic reentrant features and triple points are predicted, and each dynamic phase has unique localization characteristics and mechanical properties. Rods always have smaller localization lengths than spheres due to their enhanced excluded volume interactions and ability to form physical bonds. Orders of magnitude variation of the shear modulus and absolute yield stress are found which depend sensitively on rod length, mixture composition, and interparticle attractive forces.

We hope computer simulations will be performed in the near future to test our predictions. Experiments are in progress to test the theory based on model silica nanowire-nanosphere mixtures [37]. An *a priori* assessment of the accuracy of the underlying approximations of the theory is difficult. We do expect our key results are qualitatively correct given the multiple past successes of NMCT and NLE theory for spherical and nonspherical particle glasses and gels (as discussed in Secs. I and II) which were also based on RISM or OZ theory equilibrium structural input. Quantitatively, errors no doubt must be incurred for the dynamic crossover boundaries and mechanical properties, but unambiguous determination of their nature and magnitude requires future equilibrium and dynamic simulations of structure, kinetic arrest, and mechanical response. Additionally, our neglect of dynamical rod rotations is expected to lead to an overestimate of the tendency for localization. This conclusion has been explicitly established based on a more sophisticated NMCT theory for one-component fluids of rotating and translating rodlike particles [14]. But, for the even shorter uniaxial objects than presently studied systems studied in Ref. [14], it has been shown that including rotation has minor consequences, at least for the limited questions that the single particle NMCT addresses [11,14].

The present work provides a foundation to study more complex rod-sphere mixtures of both biological and synthetic

interest that include physical features such as interaction site size asymmetry, specific rod-sphere attractions, and Coulomb repulsion. The former will lead to depletion attraction effects. Exploring such additional complexity in the synthetic material context is of high interest for optimizing the structural and mechanical properties of nanoparticle inks for direct write printing applications [5]. Developing a theory of electrical conductivity for nanoparticle mixture inks is another overarching goal. Using an effective medium approach, we are in the process of establishing design rules for simultaneously optimizing electrical, mechanical, and structural material properties. The question of slow activated relaxation, and its consequences on linear and nonlinear mechanical response, remains an open area for future work. This will require the full nonlinear Langevin equation approach which for binary mixtures requires construction of a dynamic free energy surface [22] or direct numerical solution of the coupled NLEs of Eq. (11) via stochastic trajectory simulation. Finally, relaxing the dynamically nonrotating simplification may be of particular importance for low aspect ratio rods [11,14]. Attacking this problem will be informed by recent progress within the NMCT and NLE frameworks for dicolloid and other uniaxial nanoparticle suspensions [14].

APPENDIX A: CENTER-OF-MASS NMCT OF MIXTURES

Using the Mori-Zwanzig projection-operator formalism, a formally exact GLE for the CM coordinates of E species-distinct tagged particles, *one for each mixture component*, can be derived using standard statistical mechanical techniques [29,38]. Here we sketch the derivation.

The total "random force" matrix time correlation functions (memory functions) are approximately decomposed into a short time frictional force associated with (for example) binary interparticle collisions and/or solvent, and a slow contribution associated with conservative forces between particles and the longer time structural relaxation process [18]:

$$\left\langle \mathbf{R}_k^{CM}(0) \cdot \mathbf{R}_\alpha^{CM}(t) \right\rangle \cong \frac{6}{\beta} \zeta_{s,\alpha} \delta(t) \delta_{k,\alpha} + \left\langle \mathbf{F}_k^{CM}(0) \cdot \mathbf{F}_\alpha^{CM}(t) \right\rangle.$$
(A1)

Here, $\mathbf{R}_\alpha^{CM}(t)$ is the random force governed by projected dynamics at time t, $\mathbf{F}_\alpha^{CM}(t)$ is the CM force on a particle of species α at time t due to all interparticle interactions, and $\zeta_{s,\alpha}$ is the short time friction constant of species α. Using Eq. (A1) in the well-known expressions for the GLEs [29,38], and dropping the inertial term, yields

$$0 = -\zeta_{s,k} \mathbf{v}_{T,k}^{CM}(t) - \frac{\beta}{3} \int_0^t d\tau \sum_\alpha^E \left\langle \mathbf{F}_k^{CM} \cdot \mathbf{F}_\alpha^{CM}(\tau) \right\rangle \mathbf{v}_{T,\alpha}^{CM}(t-\tau)$$

$$+ \mathbf{R}_k^{CM}(t), \quad k = 1, 2, \ldots, E.$$
(A2)

In the long time limit the memory functions are nonzero if transiently localized states exist:

$$K_{k,\alpha}^\infty \equiv K_{k,\alpha}(t \to \infty) \equiv \frac{\beta}{3} \left\langle \mathbf{F}_k^{CM} \cdot \mathbf{F}_\alpha^{CM}(t \to \infty) \right\rangle. \quad \text{(A3)}$$

We adopt the Einstein amorphous solid model corresponding to particles independently vibrating in a harmonic manner [16–18]. Each particle is tethered to a spatial point via a species-dependent spring (cross force correlations are set to zero [22]) that is related to the effective forces and hence mixture structural correlations. The spring constant must be self-consistently determined with the localization length. In the long time limit one has

$$0 = -\zeta_{s,k} \mathbf{v}_{T,k}^{CM}(t) - K_{k,k}^\infty \left[\mathbf{r}_{T,k}^{CM}(t) - \mathbf{r}_{T,k}^{CM}(0) \right]$$

$$+ \mathbf{R}_k^{CM}(t), \quad k = 1, 2, \ldots, E \quad \text{(A4)}$$

MCT projection and factorization approximations are employed to compute the required spring constants. The slow variables are chosen to be the product of the tagged particle total (relevant to CM motion of present interest) site density fluctuation of type α with the total site density fluctuation of all particles of type s as

$$b_{\alpha,s}(\mathbf{r},\mathbf{r}') \equiv \sum_z^{N_\alpha} \delta\left(\mathbf{r} - \mathbf{r}_{T,\alpha}^z\right) \sum_j^{n_s} \sum_\gamma^{N_s} \delta\left(\mathbf{r}' - \mathbf{r}_{j,s}^\gamma\right)$$

$$- \left\langle \sum_z^{N_\alpha} \delta\left(\mathbf{r} - \mathbf{r}_{T,\alpha}^z\right) \sum_j^{n_s} \sum_\gamma^{N_s} \delta\left(\mathbf{r}' - \mathbf{r}_{j,s}^\gamma\right) \right\rangle,$$
(A5)

where the subscript T indicates the site z belongs to a tagged particle of type α, the lower binary indices on the coordinates in the collective density (j and s) denote particle number j of species type s, and the upper index in the collective density, γ, denotes the site number. Implementation of the projection and factorization ideas is straightforward (albeit tedious) within a Fourier representation, where $\hat{b}_{\alpha,s}(\mathbf{k},\mathbf{k}') \equiv \delta\hat{p}_{T,\alpha}(\mathbf{k})\delta\hat{c}_s(\mathbf{k}')$. Here we only sketch the main steps.

The bilinear projection operator is constructed as

$$\overline{P}_2 \equiv \frac{V^4}{(2\pi)^{12}} \int d\mathbf{k} \int d\mathbf{k}' \int d\mathbf{k}'' \int d\mathbf{k}''' \sum_{sg}^E \sum_{\lambda\gamma}^E \hat{b}_{\lambda,s}(\mathbf{k},\mathbf{k}')$$

$$\times B_{(\lambda,s)(\gamma,g)}^{-1}(\mathbf{k},\mathbf{k}',\mathbf{k}'',\mathbf{k}''') \langle \hat{b}_{\gamma,g}(\mathbf{k}'',\mathbf{k}''') \ldots \rangle, \quad \text{(A6)}$$

where $B_{(\lambda,s)(\gamma,g)}^{-1}(\mathbf{k},\mathbf{k}',\mathbf{k}'',\mathbf{k}''')$ is the matrix inverse of

$$B_{(\lambda,s)(\gamma,g)}(\mathbf{k},\mathbf{k}',\mathbf{k}'',\mathbf{k}''') \equiv \langle \hat{b}_{\lambda,s}(-\mathbf{k},-\mathbf{k}')\hat{b}_{\gamma,g}(\mathbf{k}'',\mathbf{k}''') \rangle. \quad \text{(A7)}$$

Following the standard Gaussian factorization approximation, Eq. (A7) can be factorized as

$$B_{(\lambda,s)(\gamma,g)}(\mathbf{k},\mathbf{k}',\mathbf{k}'',\mathbf{k}''') \cong \sqrt{n_s N_s n_g N_g} S_{sg}(k') N_\lambda \omega_\lambda(k) (2\pi)^6$$

$$\times V^{-2} \delta(\mathbf{k} - \mathbf{k}'') \delta(\mathbf{k}' - \mathbf{k}''') \delta_{\lambda\gamma},$$
(A8)

where $S_{sg}(k')$ is the collective static structure factor between sites of type s and g, and $\omega_\lambda(k)$ is the site-site intramolecular structure factor for a particle of type λ. Combining

Eqs. (A6)–(A8), the final projection operator is

$$\overline{P}_2 = \frac{V^2}{(2\pi)^6} \int d\mathbf{k} \int d\mathbf{k}' \sum_{sg}^{E} \sum_{\lambda\gamma}^{E} \hat{b}_{\lambda,s}(\mathbf{k},\mathbf{k}')(n_s N_s n_g N_g)^{-1/2}$$
$$\times S_{sg}^{-1}(k') N_\lambda^{-1} \omega_\lambda^{-1}(k) \langle \hat{b}_{\gamma,g}(\mathbf{k},\mathbf{k}') \ldots \rangle \delta_{\lambda\gamma}, \quad \text{(A9)}$$

where $S_{sg}^{-1}(k')$ and $\omega_\lambda^{-1}(k)$ are the inverse elements of the matrix $\mathbf{S}(k)$ containing $S_{sg}(k)$ and the diagonal matrix $\mathbf{\Omega}(k)$ containing $\omega_\lambda(k)$, respectively. The CM force-force correlation function matrix is then approximately computed by replacing the projected dynamics of $\mathbf{F}_\gamma^{\text{CM}}(t)$ with the real dynamics, and the forces are projected onto the subspace of slow variables:

$$K_{\alpha\gamma}(t) \cong \frac{\beta}{3} \langle \overline{P}_2 \mathbf{F}_\alpha^{\text{CM}}(0) \cdot e^{\Omega t} \overline{P}_2 \mathbf{F}_\gamma^{\text{CM}}(0) \rangle, \quad \text{(A10)}$$

where $e^{\Omega t}$ is the time evolution operator. Well-known manipulations, along with $\mathbf{F}_\alpha^{\text{CM}} = \sum_i^{N_\alpha} \mathbf{F}_\alpha^i$, can be employed to derive an explicit expression. A key intermediate step that enters the vertex calculation is

$$\mathbf{G}_{\alpha(\lambda,v)}(\mathbf{R},\mathbf{R}')$$
$$\equiv \left\langle \mathbf{F}_\alpha^{\text{CM}} \sum_n^{N_\lambda} \delta(\mathbf{R} - \mathbf{r}_{T,\lambda}^n) \sum_j^{n_v} \sum_\gamma^{N_v} \delta(\mathbf{R}' - \mathbf{r}_{j,v}^\gamma) \right\rangle$$
$$= \delta_{\alpha\lambda} \beta^{-1} N_\alpha N_v n_v V^{-1} \frac{d}{d(\mathbf{R}-\mathbf{R}')} g_{\alpha v}(|\mathbf{R}-\mathbf{R}'|), \quad \text{(A11)}$$

where the definition

$$(N_\alpha N_v)^{-1} \sum_i^{N_\alpha} \sum_\gamma^{N_v} g_{\alpha v}^{i\gamma}(|\mathbf{R}-\mathbf{R}'|) \equiv g_{\alpha v}(|\mathbf{R}-\mathbf{R}'|) \quad \text{(A12)}$$

has been used, $g_{\alpha v}(|\mathbf{R}-\mathbf{R}'|)$ is the site averaged radial distribution function between sites of type α and v, and $h_{\alpha v}(r) = g_{\alpha v}(r) - 1$. Adopting the dynamically frozen rotation model that defines the CM approach [25], the normalized site-site dynamic structure factors or propagators $\Gamma_\alpha^{ij}(k,t)$ are simply related to a single CM propagator $\Gamma_\alpha^{\text{CM}}(k,t)$, as

$$\omega_\alpha(k,t) \equiv \omega_\alpha(k)\Gamma_\alpha^{\text{CM}}(k,t). \quad \text{(A13)}$$

Collecting these results, using the RISM theory relation of Eq. (2), and other standard manipulations, the final time-dependent diagonal CM force-force correlations are

$$K_{\alpha\alpha}(t) \cong \frac{N_\alpha}{3\beta(2\pi)^3} \int d\mathbf{k} \, k^2 \omega_\alpha(k) \Gamma_\alpha^{\text{CM}}(k,t)$$
$$\times \sum_{j,k=1}^{E} C_{\alpha i}(k) \sqrt{\rho_i \rho_j} S_{ij}(k,t \to \infty) C_{j\alpha}(k). \quad \text{(A14)}$$

In the Einstein model, the CM tagged particle propagator is a Gaussian Debye-Waller factor [16–18]:

$$\Gamma_\alpha^{\text{CM}}(k,t \to \infty) \cong e^{-k^2 r_{L,\alpha}^2/6}, \quad \text{(A15)}$$

where $r_{L,\alpha}^2 = \langle [r_{L,\alpha}(t \to \infty) - r_{L,\alpha}(0)]^2 \rangle$ is the scalar localization length of the tagged particle of type α. The $S_{bz}(k,t)$'s in Eq. (A14) can be calculated as described in the prior NMCT analysis of sphere mixtures based on the Vineyard–de Gennes approach [22] that relates collective dynamics to single particle dynamics whence $S_{bz}(k,t \to \infty)$ are functions of the localization lengths $(r_{L,\beta})$.

The final step is to close Eq. (A14) for $r_{L,\alpha}$ in the long time limit under the assumption a localized state exists, i.e., $K_{\alpha\alpha}(t \to \infty) = K_{\alpha\alpha}^\infty \neq 0$. From Eq. (A4) one can then easily derive a self-consistent equation for the localization lengths, which can be written simply as

$$\tfrac{1}{2} K_{\alpha\alpha}^\infty r_{L,\alpha}^2 = \tfrac{3}{2} k_B T. \quad \text{(A16)}$$

Combining Eqs. (A14)–(A16) yields the self-consistent NMCT localization length equations

$$\frac{1}{r_{L,\alpha}^2} = \frac{N_\alpha}{9(2\pi)^3} \int d\mathbf{k} \, k^2 \omega_\alpha(k) e^{-k^2 r_{L,\alpha}^2/6} \sum_{j,k=1}^{E} C_{\alpha i}(k)$$
$$\times \sqrt{\rho_i \rho_j} S_{ij}(k,t \to \infty) C_{j\alpha}(k), \quad \alpha = 1,2,\ldots,E. \quad \text{(A17)}$$

For the binary mixture ($E = 2$), this reduces to Eq. (7) in the main text.

APPENDIX B: SHEAR MODULUS OF MOLECULAR MIXTURES

Nagele and Bergenholtz have employed the formally exact expression for the time-dependent shear modulus in conjunction with MCT projection and factorization approximations to derive an explicit formula for the elastic modulus in a localized state of mixtures of *spherical* particles [32]. Here we generalize this to molecular mixtures. The majority, but not all, of the manipulations are identical to the sphere system. Hence, we only sketch the derivation.

The time-dependent shear modulus is given by

$$\Delta\eta(t) \equiv \frac{1}{k_B T V} \langle \sigma^{xy} e^{\Omega t} \sigma^{xy} \rangle, \quad \text{(B1)}$$

where σ^{xy} is the microscopic stress tensor, and $e^{\Omega t}$ is the time evolution operator. Neglecting hydrodynamic interactions and using a simplified notation

$$\sigma^{xy} = \frac{1}{2} \sum_{i,j \to (NI)}^{N^{\text{total}}} R_{ij}^x \frac{\partial u_{ij}(\mathbf{R}_{ij})}{\partial R_{ij}^y}, \quad \text{(B2)}$$

where all the interaction sites are labeled as 1 through N^{total} and R_{ij}^x is the x component of the displacement vector between sites i and j. Note that the sum in Eq. (B2) does not include intramolecular terms, a condition indicated notationally by NI in the lowest summation label. Additionally, the labeling in Eq. (B2), and for the rest of this appendix, does not include a specific species type (e.g., 1 or 2 for rods and spheres respectively). Species type is only denoted in the summation (if necessary) by the upper N^{total} index which may contain an explicit species label. If not denoted the summation is over all possible particle sites. A collective bilinear projection operator is defined as

$$\overline{P}_3 \equiv \frac{1}{2} \frac{V}{(2\pi)^3} \int d\mathbf{k} \sum_{\alpha,\beta,\gamma,\delta}^{E} \langle \cdots A^\beta(\mathbf{k}) A^\alpha(-\mathbf{k}) \rangle$$
$$\times S_{\alpha\beta}^{(-1)}(k) S_{\beta\gamma}^{(-1)}(-k) A^\delta(\mathbf{k}) A^\gamma(-\mathbf{k}). \quad \text{(B3)}$$

where $A^\alpha(\mathbf{k}) \equiv (N_\alpha^{\text{total}})^{-1/2} \sum_{l=1}^{N_\alpha^{\text{total}}} e^{-i\mathbf{k}\cdot\mathbf{R}_j} - \sqrt{N_\alpha^{\text{total}}}(2\pi)^3 V^{-1}\delta(\mathbf{k})$. Equation (B1) is then approximated as

$$\Delta\eta(t) \cong \frac{1}{k_B T V}\langle \overline{P}_3 \sigma^{xy} e^{\Omega t} \overline{P}_3 \sigma^{xy}\rangle. \tag{B4}$$

Well-known algebraic manipulations [32] then yield

$$\Delta\eta(t) = \frac{1}{2k_B T}\frac{1}{(2\pi)^3}\int d\mathbf{k}\sum_{\alpha,\beta,\gamma,\delta}^{E}\sum_{\alpha',\beta',\gamma',\delta'}^{E} U_{\alpha\beta}(\mathbf{k})U_{\alpha'\beta'}(\mathbf{k})$$
$$\times S_{\alpha\delta}^{-1}(k)S_{\alpha'\delta'}^{-1}(k)S_{\beta\gamma}^{-1}(k)S_{\beta'\gamma'}^{-1}(k)S_{\gamma\gamma'}(k,t)S_{\delta\delta'}(k,t), \tag{B5}$$

$$U_{\alpha\beta}(\mathbf{k}) \equiv \langle \sigma^{xy} A^\alpha(\mathbf{k})A^\beta(-\mathbf{k})\rangle. \tag{B6}$$

Integrating by parts allows Eq. (B6) to be expressed as

$$U_{\alpha\beta}(\mathbf{k}) = k_B T \frac{1}{2}\sum_{i,j\to(NI)}^{N^{\text{total}}}\left\langle \frac{\partial}{\partial R_{ij}^y} R_{ij}^x A^\alpha(\mathbf{k})A^\beta(-\mathbf{k})\right\rangle. \tag{B7}$$

Equation (B7) contains two different types of contributions: (1) $\alpha = \beta$, and (2) $\alpha \neq \beta$. For the latter, one recovers the well-known result [32]:

$$U_{\alpha\beta}(\mathbf{k}) = k_B T \frac{k_x k_y}{k}\frac{d}{dk}S_{\alpha\beta}(k). \tag{B8}$$

When $\alpha = \beta$, static collective structure factors cannot enter as they contain intramolecular correlations and there are no single molecule stresses. Straightforward analysis yields

$$U_{\alpha\alpha}(\mathbf{k}) = k_B T \frac{1}{2}\sum_{i,j\to(NI)}^{N^{\text{total}}}\left\langle \frac{\partial}{\partial R_{ij}^y} R_{ij}^x \frac{1}{N_\alpha^{\text{total}}}\sum_{zx}^{N_\alpha^{\text{total}}} e^{i\mathbf{k}\cdot\mathbf{R}_{zx}}\right\rangle$$
$$= k_y \frac{d}{dk_x}\left\langle \frac{1}{N_\alpha^{\text{total}}}\sum_{i,j\to(NI)}^{N_\alpha^{\text{total}}} e^{i\mathbf{k}\cdot\mathbf{R}_{ij}^\alpha}\right\rangle$$
$$= k_y \frac{d}{dk_x}\rho_\alpha h_{\alpha\alpha}(k)$$
$$= k_B T \rho_\alpha \frac{k_x k_y}{k}\frac{d}{dk}h_{\alpha\alpha}(k) \tag{B9}$$

which is purely of intermolecular force origin. The final expression for the shear viscosity is thus

$$\Delta\eta(t) = \frac{k_B T}{60\pi^2}\int_0^\infty dk k^4 \sum_{\alpha,\beta,\gamma,\delta}^{E}\sum_{\alpha',\beta',\gamma',\delta'}^{E}\left[\sqrt{\rho_\alpha\rho_\beta}\frac{d}{dk}h_{\alpha\beta}(k)\right]$$
$$\times S_{\alpha\delta}^{-1}(k)\left[\sqrt{\rho_{\alpha'}\rho_{\beta'}}\frac{d}{dk}h_{\alpha'\beta'}(k)\right]$$
$$\times S_{\alpha'\delta'}^{-1}(k)S_{\beta\gamma}^{-1}(k)S_{\beta'\gamma'}^{-1}(k)S_{\gamma\gamma'}(k,t)S_{\delta\delta'}(k,t). \tag{B10}$$

In an ideal localized state the elastic modulus is then given by $\Delta\eta(t\to\infty) = G'$.

[1] R. G. Larson, *The Structure and Rheology of Complex Fluids* (Oxford University Press, Oxford, 1999); W. Russel, D. A. Saville, and W. R. Schowalter, *Colloidal Dispersions* (Cambridge University Press, Cambridge, England, 1989).

[2] P. Nelson, *Biological Physics: Energy, Information, Life* (W. H. Freeman, New York, 2008).

[3] M. J. Solomon and P. T. Spicer, Soft Matter **6**, 1391 (2010).

[4] A. Mohraz, E. R. Weeks, and J. A. Lewis, Phys. Rev. E **77**, 060403(R) (2008).

[5] J. A. Lewis, Adv. Funct. Mater. **16**, 2193 (2006); B. Y. Ahn, E. B. Duoss, M. J. Motala, X. Guo, S. Park, Y. Xiong, J. Yoon, R. G. Nuzzo, J. A. Rogers, and J. A. Lewis, Science **20**, 1590 (2009).

[6] E. Zaccarelli, J. Phys.: Condens. Matter **19**, 323 (2007).

[7] K. Dawson, G. Foffi, M. Fuchs, W. Gotze, F. Sciortino, M. Sperl, P. Tartaglia, T. Voightmann, and E. Zaccarelli, Phys. Rev. E **63**, 011401 (2000).

[8] E. Zaccarelli and W. C. K. Poon, Proc. Natl. Acad. Sci. USA **106**, 15203 (2009).

[9] K. N. Pham, A. M. Puertas, J. Bergenholtz, S. U. Egelhassf, A. Moussaid, P. N. Pusey, A. B. Schofield, M. E. Cates, M. Fuchs, and W. C. K. Poon, Science **296**, 104 (2002).

[10] M. Tripathy and K. S. Schweizer, Phys. Rev. E **83**, 041406 (2011); **83**, 041407 (2011).

[11] R. C. Kramb, R. Zhang, K. S. Schweizer, and C. F. Zukoski, J. Chem. Phys. **134**, 014503 (2011).

[12] M. Letz, R. Schilling, and A. Latz, Phys. Rev. E **62**, 5173 (2000).

[13] S. H. Chong and W. Gotze, Phys. Rev. E **65**, 041503 (2002).

[14] R. Zhang and K. S. Schweizer, J. Chem. Phys. **136**, 154902 (2012); Phys. Rev. E **83**, 060502(R) (2011); **80**, 011502 (2009).

[15] R. C. Kramb, R. Zhang, K. S. Schweizer, and C. F. Zukoski, Phys. Rev. Lett. **105**, 055702 (2010).

[16] T. R. Kirkpatrick and P. G. Wolynes, Phys. Rev. A **35**, 3072 (1987).

[17] K. S. Schweizer and E. J. Saltzman, J. Chem. Phys. **119**, 1181 (2003).

[18] K. S. Schweizer, J. Chem. Phys. **123**, 244501 (2005).

[19] W. Gotze, *Complex Dynamics of Glass-Forming Liquids: A Mode Coupling Theory* (Oxford University Press, Oxford, 2009).

[20] D. R. Reichman and P. Charbonneau, J. Stat. Mech. (2005) P05013.

[21] W. Götze and L. Sjogren, Rep. Prog. Phys. **55**, 241 (1992).

[22] D. C. Viehman and K. S. Schweizer, Phys. Rev. E **78**, 051404 (2008); J. Chem. Phys. **128**, 084509 (2008).

[23] G. Foffi, W. Götze, F. Sciortino, P. Tartaglia, and Th. Voigtmann, Phys. Rev. Lett. **91**, 085701 (2003).

[24] W. Götze and Th. Voigtmann, Phys. Rev. E **67**, 021502 (2003).

[25] G. Yatsenko and K. S. Schweizer, Phys. Rev. E **76**, 041506 (2007).

[26] M. Doi and S. F. Edwards, *The Theory of Polymer Dynamics* (Oxford University Press, Oxford, 1986).

[27] R. Jadrich and K. S. Schweizer, J. Chem. Phys. **135**, 234902 (2011).

[28] K. S. Schweizer and J. G. Curro, Adv. Chem. Phys. **98**, 1 (1997).

[29] J. P. Hansen and I. R. McDonald, *Theory of Simple Liquids*, 2nd ed. (Academic Press, London, 1986).

[30] D. Chandler and H. C. Andersen, J. Chem. Phys. **57**, 1930 (1972); D. Chandler, in *Studies in Statistical Mechanics*, edited by E. W. Montroll and J. L. Lebowitz, Vol. III, (North Holland, Amsterdam, 1982), p. 274, and references cited therein; D. M. Richardson and D. Chandler, J. Chem. Phys. **80**, 4464 (1984).

[31] Y. L. Chen and K. S. Schweizer, J. Chem. Phys. **120**, 7212 (2004).

[32] G. Nägele and J. Bergenholtz, J. Chem. Phys. **108**, 9893 (1998).

[33] V. Kobelev and K. S. Schweizer, Phys. Rev. E **71**, 021401 (2005).

[34] R. C. Kramb and C. F. Zukoski, J. Phys.: Condens. Matter **23**, 035102 (2011).

[35] K. S. Schweizer and G. Yatsenko, J. Chem. Phys. **127**, 164505 (2007); K. S. Schweizer, *ibid.* **127**, 164506 (2007).

[36] H. Guo, S. Ramakrishnan, J. L. Harden, and R. L. Leheny, Phys. Rev. E **81**, 050401 (2010); S. Ramakrishnan, V. Gopalakrishnan, and C. F. Zukoski, Langmuir **21**, 9917 (2005).

[37] A. Russo and J. A. Lewis (unpublished).

[38] R. Zwanzig, *Nonequilibrium Statistical Mechanics* (Oxford University Press, Oxford, 2001).